Proceedings of the 9th World Congress on Momentum, Heat and Mass Transfer (MHMT 2024)
London, United Kingdom – April 11 – 13, 2024
Paper No. ICMFHT 153
DOI: 10.11159/icmfht24.153

Experimental Characterization of Heat and Mass Transfer in Cryogenic Storage Tanks

Pedro Afonso Marques[1,2], Alessia Simonini[1], Mathieu Delsipée[1], Miguel Alfonso Mendez[1]
[1]von Karman Institute for Fluid Dynamics
Waterloosesteenweg 72, Sint-Genesius-Rode, Belgium
pedro.marques@vki.ac.be Second.Author@institution.org
[2]Transferts, Interfaces Et Procédés (TIPs), Université Libre de Bruxelles
Av. Franklin Roosevelt 50, Brussels, Belgium

Abstract **–** Cryogenic storage requires complex thermal management systems and advanced control strategies to minimize boil-off. However, these require a fundamental understanding of the underlying heat and mass transfer mechanisms to predict the system's thermodynamic evolution accurately. In this scope, this work presents the experimental characterization of heat and mass transfer in a cryogenic upright cylindrical reservoir. The experimental campaign is performed with liquid nitrogen under three main scenarios: (1) active pressurization, (2) post-pressurization relaxation, and (3) sloshing. The experimental setup consists of four fundamental components: a 'donor' tank filled with room-temperature nitrogen vapour, a 'receiver' tank partially filled with LN2, a pressurizing line connecting these two, and a bath cryostat. The setup is fully instrumented, including a series of thermo-diodes to measure the temperature distribution along the gas, liquid, and solid surfaces, fast-response pressure sensors, and a mass-flow controller to finely regulate the pressurization rates. Moreover, the 'receiver' tank is built from quartz, allowing for optical access during all stages of the experiment. Our findings demonstrate the impact of varying the pressurization rates on the liquid's temperature distribution and the subsequent pressure relaxation. Furthermore, we directly compare the disruptive impact of sloshing on the thermodynamic trajectory of the system by combining high-speed image acquisitions with pressure and temperature readings.

Keywords**:** Cryogenic, Experiments, Long-term storage, Sloshing

1. Introduction

The ongoing energy crisis has shifted many industries towards sustainable energy systems. Among these, cryogenic propellants like liquid hydrogen (LH2) and liquefied natural gas (LNG) are particularly promising. Stored at exceptionally low temperatures to maximize their energy density [1] and traditionally associated with space propulsion, cryogenic fuels are remarkable given their low pollutant emissions [2] and high specific energy [1]. These features are uniquely advantageous for industries such as aeronautics [3] and shipping [4].

However, cryogenic storage requires complex thermal management systems [5] to maintain the required operating temperatures (e.g., -170 °C for LNG and -250 °C for LH2). Since no insulating system can entirely prevent heat exchanges with the surroundings, some of the fuel unavoidably evaporates over time, increasing the tank pressure [3]. Moreover, when tanks are installed on vehicles, their manoeuvres, vibrations, and accelerations induce sloshing. Sloshing, defined as the movement of the free liquid surface, can harm the vehicle's stability and manoeuvrability [6] while increasing heat and mass transfer rates between the liquid and ullage gasses [7]. Consequently, the tank's pressure varies substantially, causing structural instabilities in the shell and hindering the smooth distribution of fuel to the engine [7]. These harsh thermo-hydraulic effects pose significant challenges to any application requiring long holding times. To manage such effects sophisticated insulation methods and advanced control strategies are required [5]. However, these methods require robust modelling of the underlying heat and mass transfer mechanisms to accurately predict the system's thermodynamic trajectory.

Integrated within a larger research effort to characterize the thermodynamic response of cryogenic tanks, this paper presents the experimental characterization of heat and mass transfer in a cryogenic upright cylindrical reservoir. The experimental campaign, performed in the von Karman Institute's CryME (Cryogenic Microgravity Experiments) cryostat, comprises three major operating scenarios for cryogenic tanks: (1) active pressurization, (2) post-pressurization relaxation, and (3) sloshing. By varying parameters in each scenario (e.g. the pressurization rates, maximum pressure, relaxation, and sloshing excitation), we generate an extensive database from which we extract the underlying dynamics of the system. Hence,

this work constitutes an initial foundation for future studies to derive novel modelling approaches and validate high-fidelity simulations.

2. Methodology

2.1. Experimental setup

The experimental setup comprises four major components: a 'donor' tank carrying room-temperature nitrogen vapour, a ‘receiver’ tank partly filled with LN_2, a bath cryostat, and a pressurization line connecting the first two components. Figure 1 presents the setup as assembled in the laboratory.

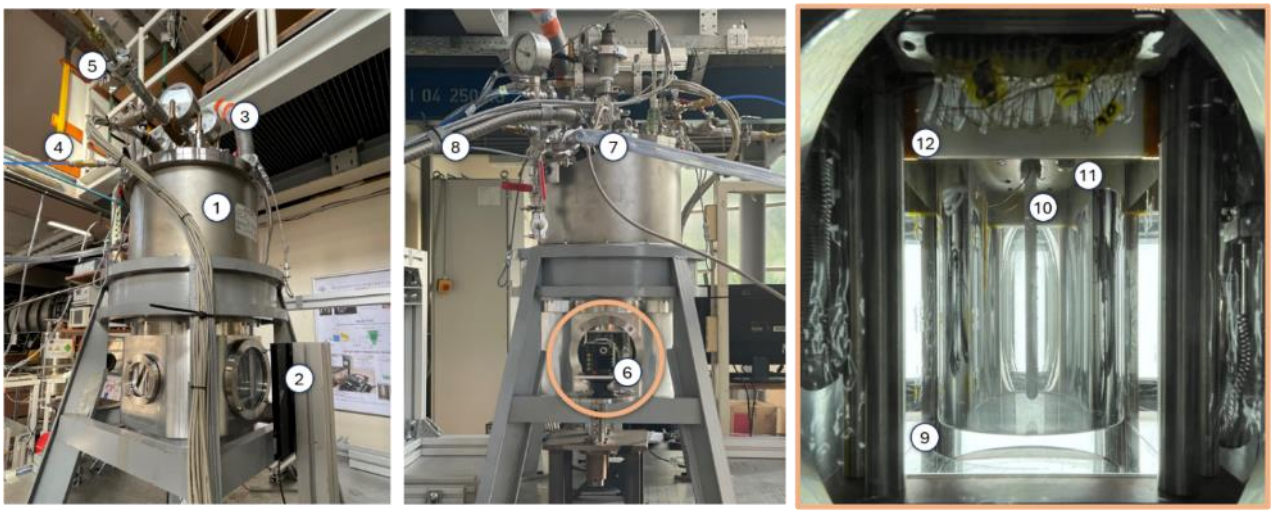

Fig. 1: Experimental setup assembled on the von Karman Institute’s SHAKESPEARE facility, with the CryME bath cryostat (left, and centre) and the cryogenic ‘receiver’ tank (right). The numbered labels indicate: (1) CryME bath cryostat, (2) diffusive screen, (3) cryostat LN2 filling port, (4) ‘donor’ to ‘receiver’ pressurization line, (5) ‘receiver’ vacuum line, (6) high-speed camera, (7) cryostat exhaust port, (8) cryostat external jacket vacuum port, (9) quartz ‘receiver’ tank, (10) thermal probe, (11) diffuser, (12) heating elements.

The ‘donor’ tank is a metal-sealed vessel pressurised at five bara with room temperature gas nitrogen. Before filling, the tank is vacuumed and purged with nitrogen to remove other gases and contaminants. We measure its temperature through a type K thermocouple and its pressure with an AMS 6916-1000-D sensor. The pressurisation from the ‘donor’ to the ‘receiver’ is performed with a Bronkhorst EL-FLOW F-201CV mass flow controller. Once the controller valve is open, the warm vapour is discharged to the ‘receiver’ through a diffuser that directs the gas radially, minimising its impact onto the free surface of the liquid. The ‘receiver’ tank is installed in a thermally controlled environment, i.e. a cryostat. The cryostat comprises four main volumes: the LN2 reservoir; the sample space; the heat exchanger; and the vacuum chamber. The reservoir chills down the sample space through the heat exchanger. The working temperature is finely controlled between 75 K and 85 K. The sample space is initially filled with gaseous helium at 0.3 bara, maximising its thermal conductivity and temperature uniformity. Once the desired working temperature is reached, the helium is removed from the volume, keeping it under vacuum.

The cryogenic ‘receiver’ tank is mounted in the sample space and attached to the heat exchanger. The tank is built from quartz, allowing for optical access and image acquisition. It consists of a rectangular cuboid with outer dimensions of 100 mm by 100 mm and 134 mm, drilled with a circular hole with a diameter of 80 mm and a depth of 124 mm. This assembly is fully instrumented. A fast-response Kulite CTL-190 sensor measures the vapour pressure, while a central probe with nine Lakeshore DT-670-SD thermo-diodes acquires the temperature distribution along the gas and liquid regions. To minimise the thermal conduction on the sensing surface of the diodes, the probe is composed of two layers: an inner structural one made of stainless steel and an outer one of Macor. The inside of the probe is hollow to pass the

wires of the diodes and avoid disturbing the flow. The outer surface of the probe is machined with several steps on which the diodes are attached, keeping the sensing surfaces in contact with the fluid. The wires of each diode are carefully routed routed along the probe, threaded through holes located at each step, and passed to the inner hollow cavity. Moreover, we we employ seven additional diodes on the inner and outer solid surfaces to estimate the heat fluxes to the fluid during the the experiments. Table 1 presents the relevant information regarding the thermo-diodes, including the sensors' naming, vertical coordinates relative to the inner bottom surface of the quartz, and the region in which their sensing surfaces are attached when the interface is stationary for the nominal fill level of 60 mm.

Table 1: Location of the thermos-diodes sorted by their sensor identification numbers. The vertical coordinate z is measured from the lower inner surface of the quartz 'receiver' tank. The position sensing surface is provided at the nominal fill level of 60 mm.

Sensor	D01	D02	D03	D04	D05	D06	D07	D08	D09	D10	D12	D13	D14
***z*[mm]**	102	10	134	106	85	68	58	54	45	20	85	45	10
Sensing surface	Inner wall	Inner wall	Top wall	Gas	Gas	Gas	Liq.	Liq.	Liq.	Liq.	Ext. wall	Ext. wall	Ext. wall

Four Minco HAP6945 polyimide thermofoil heaters are mounted in the upper portion of the tank to create a stable thermal gradient along the walls and to supply heat ingress. The power the heating elements supply is finely controlled using a CryoVac TIC 500 controller coupled with a thermo-diode to impose fixed temperature conditions at the heaters' surfaces. Moreover, given the optical access provided by the cryostat and the 'receiver' tank, we acquire images of the flow using a JAI SP-1200M-CXP4 camera. The fluid is illuminated from the back through a high-intensity TH2- 200X150SW diffusive LED screen.

The cryostat containing the 'receiver' tank is mounted on the SHAKESPEARE (SHaking Apparatus for Kinetic Experiments of Sloshing Projects with EArthquake Reproduction) facility in the von Karman Institute. The facility comprises three sliding modules which allow for complex three-dimensional excitations with controlled amplitudes and frequencies. The sloshing excitations are recorded via a triaxial Endevco Model 7298 accelerometer and an ODS-30 optical displacement sensor.

2.2. Experimental procedure and matrix

Before starting the experiments, we purge all volumes within the cryostat, buffer tank, and pressurization line with gaseous nitrogen. Then, we repeat this process for the 'donor' tank and fill it with room temperature gas nitrogen to 5 bara. Subsequently, the cryostat is chilled down to 77 K, and its reservoir is filled with LN2 at this temperature. Once the reservoir's level sensor indicates it is full, we fill the 'receiver' by slowly opening the filling valve. Here, the liquid level is adjusted optically according to the relative position of the interface with respect to the thermo-diodes in the central probe. This task is aided by a millimetric grid attached to the lateral edge of the quartz, allowing for finer control of the liquid level to a depth of 60 mm (i.e., $H_l/R = 1.5$).

All setup components are prepared to start the experiments at this stage, and we start acquiring the sensor data. The first step is to provide heat ingress to the system and create a vertical thermal stratification in the receiver by regulating the imposed temperature in the TIC500 controller. This stratification requires between 30 minutes and one hour for prescribed temperatures of 81 to 85 K, respectively.

We mix the fluid to ensure repeatability between tests by inducing a swirl sloshing excitation for 2 minutes. This mixing ensures that both the gas and liquid collapse to a uniform temperature. Then, the ullage of the 'receiver' is vacuumed to further correct the fill level and to cool down the liquid to 76 K. Once this temperature is reached, the fluid is mixed again by swirling it for 2 minutes. Then, the system is undisturbed for 2 minutes, allowing the thermal stratification to set in the gas and liquid. Subsequently, we open the mass flow controller's regulating valve to pressurize the 'receiver using the room temperature vapour from the 'donor'. Since the 'receiver' is always pressurized to 2 bara, the duration of this step depends on the selected mass flow. Once the maximum pressure is reached, the regulating valve is closed, and the system enters the relaxation phase until the pressure reaches 1.7 bara. Lastly, the 'receiver' tank is disturbed by imposing a harmonic forcing

motion around the first asymmetrical natural frequency [6]. By varying the forcing amplitude and frequency, we achieve sloshing excitations in the planar, swirl and chaotic wave regimes [8]. Following this, we enter a 15-minute break phase, allowing the system to evolve passively. Once this time has elapsed, we stop acquiring the sensor data and repeat the procedure for the following experiment.

The experimental matrix is presented in Table 3. The test name starts with the letter 'T' followed by the number of experiment. The results shown in this paper constitute only some of the experiments acquired during the experimental campaign. The focus of each experiment is numbered between (1) – (3) for: (1) active pressurization, (2) post-pressurization relaxation, and (3) sloshing. The system parameters before pressurization are shown in the table with the index "bp". The temperatures in each control volume are obtained by averaging the sensor readings of thermo-diodes D04 – D06 for the gas $T_{g,bp}$, D07 – D10 for the liquid $T_{l,bp}$, and D12 – D14 for the solid $T_{w,bp}$. The pressurization mass flow rate is displayed as a percentage of the maximum flow rate measured by the instrument, which is 0.188 g/s.

Table 3: Experimental matrix summarizing the operating stage of each experiment, alongside its initial conditions.

Test ID	Focus	$T_{g,bp}$ [K]	$T_{l,bp}$ [K]	$T_{wg,bp}$ [K]	$T_{wl,bp}$ [K]	p_{bp} [bara]	p_{max} [bara]	$\dot{m}$ [%]	Sloshing
T17	(1), (2)	78.95	77.31	80.19	77.38	1.04	1.94	20	-
T18	(1), (2)	79.31	77.35	80.35	77.36	1.06	1.94	5	-
T19	(1), (2)	79.11	77.11	80.17	77.19	1.04	1.98	100	-
T35	(3)	78.90	77.02	80.02	76.98	1.05	1.94	20	Planar
T38	(3)	78.88	76.72	80.08	76.76	1.03	1.94	20	Swirl
T43	(3)	79.35	77.18	80.41	77.16	1.09	1.94	20	Chaotic

3. Results and discussion

3.1. Active pressurization and relaxation

This section compares the impact of varying the pressurization rates on the temperature distribution in the liquid phase, as well as the pressure relaxation. In Figure 3, we compare three different flow rates imposed by the mass-flow controller: 0.009 g/s, 0.038 g/s, and 0.188 g/s. The zero of the time-axis coincides with the end of the pressurization.

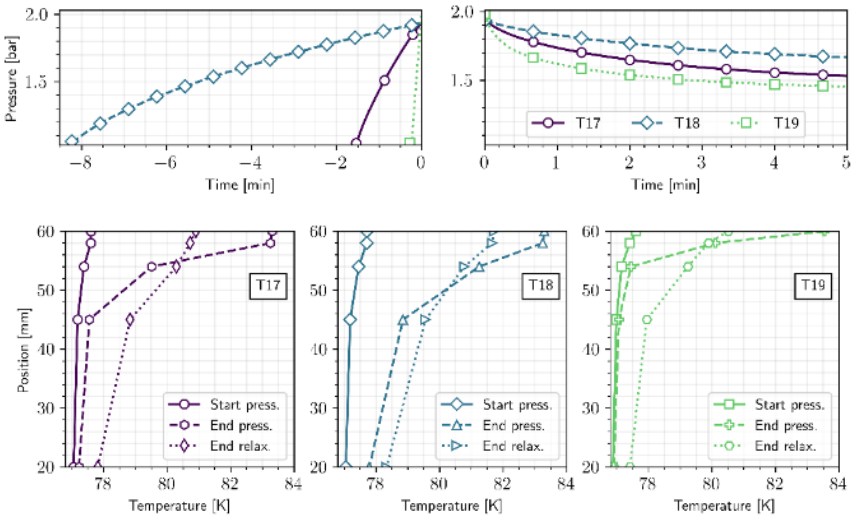

Fig. 3: Pressure time-series (top) and temperature profiles in the liquid (bottom) during the pressurization and relaxation stages. The pressure plots are divided in two stages: pressurization (top left) and relaxation (top right). The temperature plots are divided for each experiment: T17 with $\dot{m} = 0.038$ g/s (bottom left), T18 with $\dot{m} = 0.009$ g/s (bottom centre), and T19 with $\dot{m} = 0.188$ g/s (bottom

right). The corresponding thermal profiles are shown before the pressurization (solid line with circular markers), at its end (dashed line with square markers), and 5 minutes into the relaxation stage (dotted line with diamond markers).

Focusing first on the pressure evolution, as the injected flow rate increases, so does the magnitude of the pressure drop drop in the relaxation stage. Particularly, in T19, the pressure only decreased by 13.9%, whereas in T19, the drop nearly doubled (26.7%). By integrating the measured mass flow rate over the pressurisation period, we find that the injected vapour vapour mass in T17 and T18 was similar: 0.073 g and 0.081 g, respectively. Yet in T19, the value increased to 0.112 g. While While these variations can be partly attributed to slight differences in each test's initial and boundary conditions, our findings suggest a sweet spot regarding the pressurisation rate to minimise condensation. Remarkably, even though the pressurisation in T19 was the shortest, lasting only 9 seconds, its high injected vapour mass suggests considerable condensation occurred during this test's pressurisation phase.

We complement these findings by analysing the evolution of the thermal profiles. Across all cases, the liquid has a clear thermal stratification at the end of the pressurisation. Moreover, we denote the formation of a thermal boundary layer under the interface, which is sharpest for T19 and smoothest for T18. The growth of this layer is governed by the temperature increase of the interface during the pressurisation and by the diffusive and convective heat fluxes in the liquid [9]. Therefore, if these fluxes are identical across all test cases, the thickness of this layer should increase proportionally to the pressurisation duration. During the relaxation stage, the bulk temperature increases, measured by D09 and D10. However, the fluid near the interface, measured by diodes D07 and D08, cools down. This cooling is partly attributed to thermal diffusion within the liquid and the interface temperature's evolution. Since the 'receiver' tank is a single-species system, there is a direct relationship between its pressure and the interface temperature. Thus, as the vapour loses thermal energy to the surrounding walls and liquid, the interface cools down, reflecting the change in vapour pressure.

3.2. Sloshing

In this section, we compare the influence of different sloshing excitations (i.e., planar, chaotic and swirl) on the thermodynamic trajectory of the 'receiver' tank. Figure 4 presents representative snapshots of each forcing excitation (left) and the temporal evolution of the ullage pressure for each of them (right). Figure 5 supplements the investigation by showing each sloshing case's ullage and liquid temperature time series. Here, the zero of the time-axis coincides with the start of forcing motion.

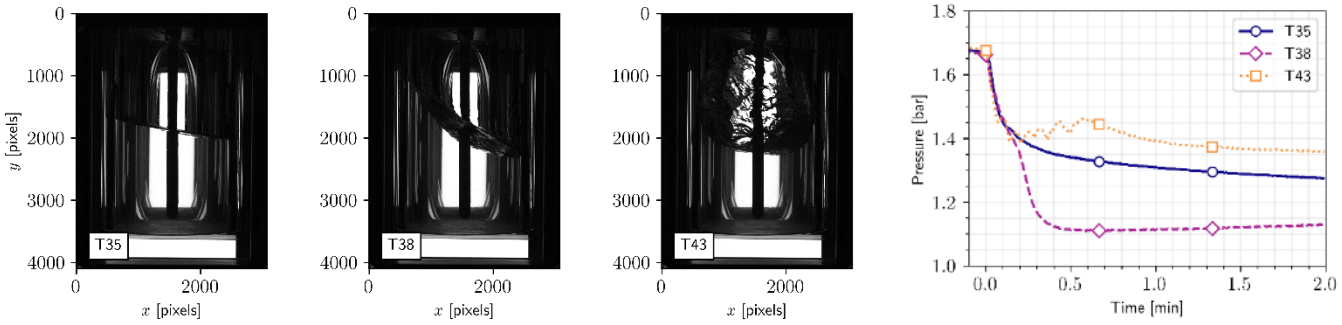

Fig. 4: Snapshots of the fluid motion in each experiment (left) and pressure time-series for varying sloshing disturbances (right). The experiments were carried out in the planar (T35), swirl (T38), and chaotic (T43) wave regimes.

We start by analysing the time series of the ullage pressure. All test cases produced identical pressure evolutions during the first 5 seconds of excitation. This matching results from similar transient dynamics of the fluid from stationary conditions [10]. Thus, once the characteristic motion of each case sets in, the differences among them become apparent. The planar excitation (T35) produced a smooth pressure drop, resembling an exponential decay. On the other hand, the swirl case (T38) generated the steepest drop, decreasing its pressure by 33 % within 41 seconds. Lastly, the chaotic test (T43) originated a

noisy signal with many peaks and valleys throughout its history, yielding the lowest pressure drop across the three experiments (19 %).

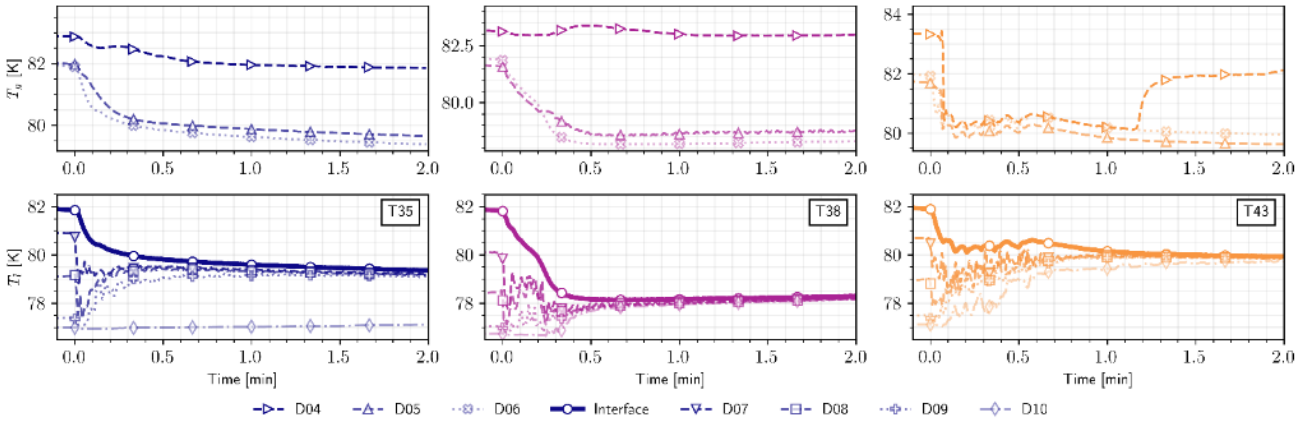

Fig. 5: Temperature time-series during sloshing (t = 0) for the diodes located in the gas (upper plots) and liquid (lower plots) regions. Each column corresponds to one test case: T35 (left), T38 (centre), and T43 (right).

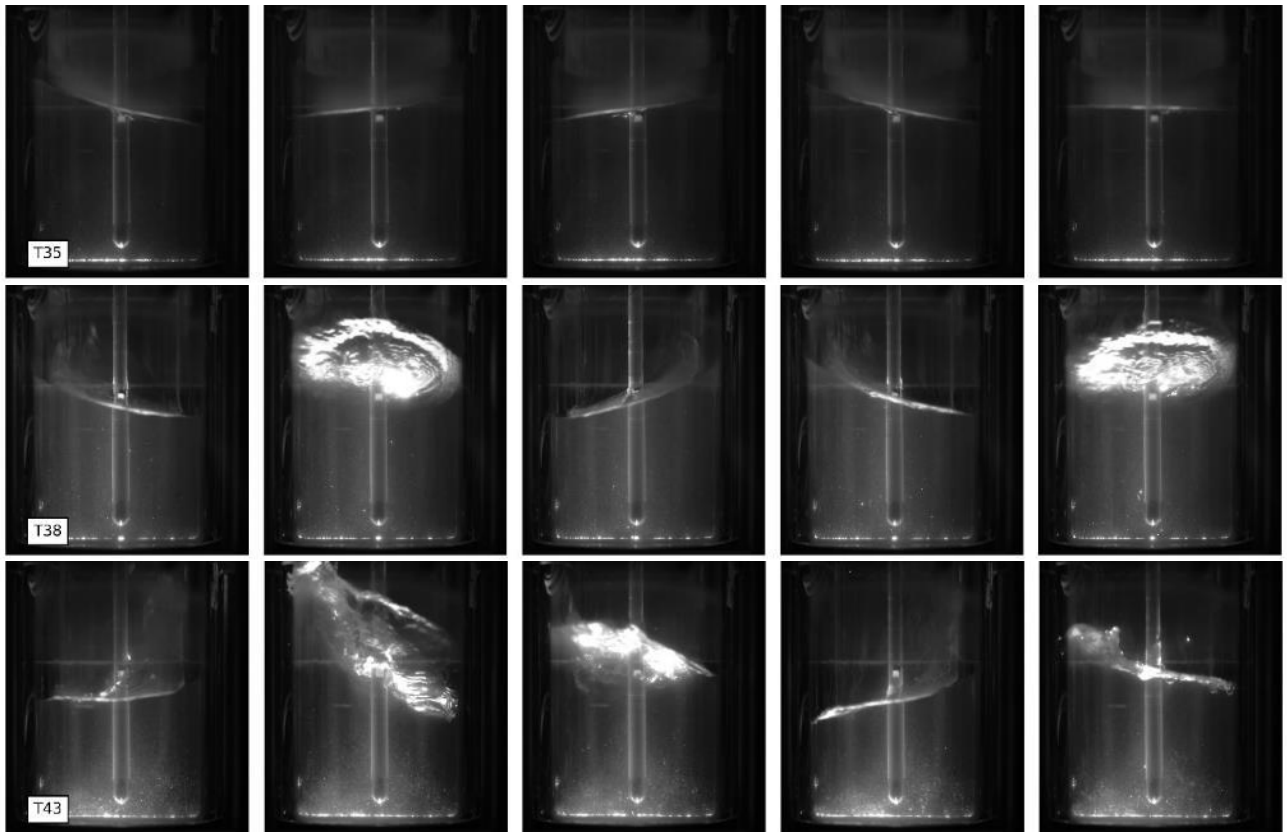

Fig. 6: Snapshots of the fluid motion in each experiment, illuminated by a laser sheet from the bottom of the tank. The first row refers to the planar case (T35), the central one to the swirl (T38), and the bottom one to the chaotic one (T43).

We gain further insight into the pressure evolutions by relating the temperature evolutions in Figure 5 with snapshots of the fluid motion displayed in Figure 6. Case T35, in the planar waves regime, is characterized by its harmonic motion with a flat interface. This sloshing mixes the temperature in the vicinity of the interface, reaching sensor D09 (45mm from the bottom), but fails to impact D10 (20 mm from the bottom), which only increases its temperature by 1% throughout the entire excitation. On the side of the gas, sensors D05 and D06 follow the same trend as the sensors under the interface, although the impact on D04 is less evident.

Remarkably, case T38, in the swirl regime, yields a complete mixing of the temperature field in the 'receiver' tank. Consequently, after one minute of sloshing, all diodes except D04 are within 3.6 % of each other, around 78.1 K. This strong mixing results from the strong rotational fluxes shown by the swirl regime. As shown in Figure 6, the resulting excitation is a high-amplitude rotating wave which destroys the thermally stratified field and the tank's overpressure. In closing, case T43, in the chaotic regime, is triggered near resonance conditions. The wave height increases until the moving wave's acceleration equals the gravitational forces or until it reaches the top surface of the tank, leading to wave breaking [9]. Thus, the motion is characterized by seemingly unpredictable dynamics. Due to the high amplitudes, the rising waves reach the tank's uppermost portions, including the top cover's lower surface. These high amplitudes produce strong convective fluxes, which reach the deepest regions in the bulk, shown by the increased temperature measured by D10 and the highest in the ullage, as reported by the sharp drop in D04. However, unlike the swirl regime, the system tends towards a higher homogenous temperature, around 80 K. This might be explained by the larger wave amplitudes, which force the liquid to extract thermal energy from hotter surfaces, thus increasing its bulk temperature and limiting the magnitude of the pressure drop.

4. Conclusion

In this work, we characterised the heat and mass transfer in a cryogenic upright cylindrical reservoir partly filled with LN2. The presented experiments comprised representative scenarios in the thermal management of cryogenic fuel tanks, including active pressurisation, relaxation and sloshing events. The setup was instrumented with an array of thermo-diodes measuring the temperature distribution in the gas, liquid and solid boundaries, high-frequency pressure sensors, and a mass flow controller to regulate the pressurisation. Furthermore, we employed a high-speed camera to capture the fluid dynamics during the experiments.

Each experiment was composed of three main stages: (1) active pressurisation, (2) pressure relaxation, and (3) sloshing. By varying the pressurisation rates, we found that there are consequences on the subsequent pressure relaxation and the thermal profiles developed in the fluid. Low pressurisation rates allow for the diffusive fluxes to travel from the warm vapour to the colder solid and liquid volumes. As a result, this case is characterised by a small relaxation (i.e., reduction) of the pressure. On the other hand, fast pressurisation rates do not offer enough time for the thermal information to propagate along the boundaries surrounding the ullage. As a result, we retrieve a sharp thermal boundary layer under the gas-liquid interface. Moreover, given the sharp injection of warm gas into a relatively colder environment, a significant amount of condensation is produced. Accordingly, the subsequent relaxation is significantly larger than in the previous case. This difference is partly attributed to the higher condensation rates and more thermal energy transferred from the warm ullage to the solid and liquid.

This work compared the impact of different sloshing dynamics on the thermodynamic trajectory of the pressurised tank. By varying the excitation parameters, we achieved planar, swirl, and chaotic wave regimes. Then, we compared the measured pressure and temperature data with high-speed image acquisition. The planar waves case was characterised by a nearly flat interface which moved along the excitation direction according to a harmonic motion. Here, the pressure decreased steadily according to a nearly exponential decay. Moreover, the temperature in the vicinity of the interface was fully mixed, leading to a decrease in the interface temperature and an increase in the bulk. However, the velocity field produced by this wave regime was not enough to reach the deepest regions of the bulk, which remained subcooled throughout the experiment. On the other hand, the swirl case produced a stable and high-amplitude rotating wave, which effectively mixed the entire fluid, leading to a massive pressure drop (33% within 41 seconds). As a result of this mixing, the subcooled bulk was able to effectively extract energy from the warmer ullage, cooling it by over 3 K, and leading to a uniform temperature inside the tank. Lastly, the chaotic case produced oscillations in the pressure signal, yielding the lowest pressure drop out of the three

scenarios, albeit with a complete mixing of the temperature field. This case showed seemingly unpredictable high-amplitude waves reaching the tank's uppermost regions. As a result, the moving fluid could extract thermal energy from the highest temperature regions in the setup. In turn, this led to an effective heating of the bulk temperature, which mitigated the magnitude of the pressure drop.

The presented results constitute the first steps of analysing the data acquired in the latest cryogenic experimental campaign carried out at the von Karman Institute. Our findings lay a solid foundation for subsequent investigations to further characterise the heat and mass transfer dynamics in cryogenic storage. Furthermore, this extensive database comprises a valuable resource that can be used to derive novel modelling approaches, opening the door to advanced control strategies such as model predictive control.

Acknowledgements

This work was supported by the European Space Agency (ESA) in the framework of the GSTP-SLOSHII project with reference number 4000129315/19/NL/MG. The authors gratefully acknowledge the financial support of the 'Fonds de la Recherche Scientifique (F.R.S. - FNRS)' for the FRIA grant with reference FC47297 supporting the Ph.D. of Mr. Marques.

References

[1] P. Fortescue, J. Stark, and G. Swinerd, Spacecraft systems engineering, 3rd ed. West Sussex, England: John Wiley & Sons Ltd., 2003.

[2] M. Ball and M. Wietschel, "The future of hydrogen – opportunities and challenges," International Journal of Hydrogen Energy, vol. 34, no. 2, pp. 615–627, Jan. 2009, doi: 10.1016/j.ijhydene.2008.11.014.

[3] G.-M. Jeon, J.-C. Park, and S. Choi, "Multiphase-thermal simulation on BOG/BOR estimation due to phase change in cryogenic liquid storage tanks," Applied Thermal Engineering, vol. 184, p. 116264, Feb. 2021, doi: 10.1016/j.applthermaleng.2020.116264.

[4] D. Verstraete, P. Hendrick, P. Pilidis, and K. Ramsden, "Hydrogen fuel tanks for subsonic transport aircraft," International Journal of Hydrogen Energy, vol. 35, no. 20, pp. 11085–11098, Oct. 2010, doi: 10.1016/j.ijhydene.2010.06.060.

[5] S. Barsi, "Ventless pressure control of cryogenic storage tanks," Case Western Reserve University, Cleveland, Ohio, United States of America, 2010.

[6] R. A. Ibrahim, Liquid Sloshing Dynamics: Theory and Applications. New York, United States of America: Cambridge University Press, 2005.

[7] M. E. Moran, N. B. McNelis, M. T. Kudlac, M. S. Haberbusch, and G. A. Satornino, "Experimental results of hydrogen slosh in a 62 cubic foot (1750 liter) tank," presented at the 30th Joint Propulsion Conference cosponsored by AIAA, ASME, SAE, and ASEE, Indianapolis, Indiana, 1994.

[9] C. Ludwig, M. E. Dreyer, and E. J. Hopfinger, "Pressure variations in a cryogenic liquid storage tank subjected to periodic excitations," International Journal of Heat and Mass Transfer, vol. 66, pp. 223–234, Nov. 2013, doi: 10.1016/j.ijheatmasstransfer.2013.06.072.

[10] [1] P. A. Marques, A. Simonini, L. Peveroni, and M. A. Mendez, "Experimental analysis of heat and mass transfer in non-isothermal sloshing using a model-based inverse method," Applied Thermal Engineering, vol. 231, p. 120871, Aug. 2023, doi: 10.1016/j.applthermaleng.2023.120871.